Estuaries Vol. 26, No. 3, p. 651–669 June 2003

A Modeling Study of the Satilla River Estuary, Georgia. I: Flooding-Drying Process and Water Exchange over the Salt Marsh-Estuary-Shelf Complex

LIANYUAN ZHENG[1], CHANGSHENG CHEN[2,*], and HEDONG LIU[2]

[1] *College of Marine Science, University of South Florida, St. Petersburg, Florida 33701*
[2] *School for Marine Sciences and Technology, University of Massachusetts-Dartmouth, New Bedford, Massachusetts 02744*

ABSTRACT: The flooding-drying process over the intertidal zone of the Satilla River estuary of Georgia was examined using a three-dimensional (3-D) primitive equations numerical model with Mellor and Yamada's (1982) level 2.5 turbulent closure scheme. The model was forced by the semi-diurnal M_2, S_2, and N_2 tides and freshwater discharge at the upstream end of the estuary. The intertidal salt marsh was treated using a 3-D wet-dry point treatment technique that was developed for the σ-coordinate transformation estuary model. Good agreement was found between model-data comparison at anchor monitoring sites and also along the estuary that suggested that the model provided a reasonable simulation of the temporal and spatial distributions of the 3-D tidal current and salinity in the Satilla River estuary. Numerical experiments have shown that the flooding-drying process plays a key role in the simulation of tidal currents in the main river channel and in water transport over the estuarine-salt marsh complex. Ignoring this process could lead to a 50% underestimation of the amplitude of tidal currents. The model results also revealed a complex spatial structure of the residual flow in the main channel of the river, with characteristics of multiple eddy-like cell circulations. These complicated residual currents are formed due to tidal rectification over variable topography with superimposition of inertial effects, asymmetry of tidal currents, and baroclinic pressure gradients. Water exchanges over the estuary-intertidal salt marsh complex are asymmetric across the estuary, and tend to vary periodically on the northern side while quickly washing out of the marsh zone on the southern side. Strong Stokes' drifting velocity was predicted in the estuary, so that the Lagrangian trajectories of particles were characterized by strong nonlinear processes that differ significantly from those estimated by the Eulerian residual currents.

Introduction

Estuaries, which include lagoons, inlets, bays, and intertidal salt marshes, occupy about 80% to 90% of the coastal area along the eastern United States (Emery 1967). Most of these estuaries have a spatial length scale of about 10 km in the horizontal and a few meters in the vertical. The Satilla River estuary, on the Georgia coast, is a typical tidally controlled estuary connected with extensive intertidal salt marshes (Fig. 1). The mean depth of this river is about 4 m but the tidal range is over 3 m during spring tide (Zheng 1999). The large ratio of surface elevation to mean water depth makes the Satilla River estuary a fully nonlinear estuarine dynamic system that must be studied using a nonlinear primitive equation model.

To simulate the water transport flushing onto and draining from salt marshes in the Satilla River estuary, a proper approach of the flooding-drying process (i.e., submergence at high water and emergence at low water) must be developed. In terms of mathematics, this seems difficult because the numerical computational domain varies with time (Cheng et al. 1993). Many attempts have been made to solve this problem in the last 20 yr and two different approaches have been developed: the moving boundary method and the wet-dry point treatment method. In the moving boundary method, the computational domain (or model grid) is reconfigured for each time step according to the boundary defined by zero total depth and a zero normal transport interface line between land and water (Lynch and Gray 1980; Johns et al. 1982; Shi 1995). Grid generation using this method would be cumbersome, particularly in an estuarine area where complex shorelines and numerous islands exist. Although this approach is conceptually applicable and has more precise computation, it has been used only for some idealized estuarine cases (Sidén and Lynch 1988; Austria and Aldama 1990).

In the wet-dry point treatment method, the numerical computational domain covers the entire intertidal area. The moving boundary between the land and water (where water flux is equal to zero) is determined for each time step by the wet-dry point treatment technique. The wet and dry points

---

* Corresponding author; e-mail: c1chen@umassd.edu.

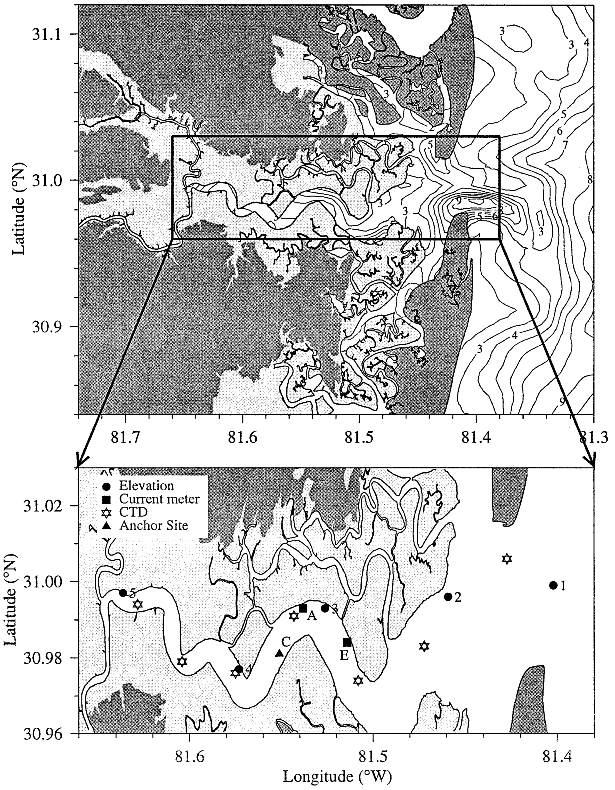

Fig. 1. Georgia coastline (upper) and the location of the Satilla River estuary (lower). The gray-filled area in the right panel is the 2-m intertidal zone. Filled squares (A and E) are the locations of the two current meter mooring sites. Filled circles are the along-river elevation measurement stations. Stars are the along-river CTD measurement stations and filled triangle (C) is the anchor site where a time series of CTD measurement was made. Water depth (m) is provided in the upper panel.

are defined using the local total depth D = H(x, y) + ζ(x, y, t) (H is the mean water depth and ζ is the surface elevation). When D is positive, it is defined as a wet point; otherwise it is a dry point. At the dry point, all the equations are treated simply by assuming the vertical eddy viscosity to be infinite and thus velocity at this point automatically disappears. This method is widely used in the depth-averaged (2-D) numerical estuarine model for the simulation of water transport over intertidal areas (Leendertse 1970, 1987; Flather and Heaps 1975; Ip et al. 1998).

Applying the wet-dry point treatment technique to a 3-D primitive equation model requires that the equations satisfy a finite value solution when the total depth D approaches zero. In the z-coordinate system, the method used in the 2-D model can be applied easily to the 3-D case without any technical difficulties (Casulli and Cheng 1991, 1992; Cheng et al. 1993; Casulli and Cattani 1994; Hervouet and Janin 1994). To ensure numerical stability, the thickness of the layer closest to the surface must be greater than the amplitude of the tidal elevation (Davies et al. 1997). This makes it difficult to use this method in a shallow estuary like the Satilla River where the average depth is about 4 m but the amplitude of tidal elevation can reach 3 m. The z-coordinate system poorly represents the varying bottom topography. The wet-dry point treatment method in such a system might not ensure mass conservation.

The σ-transformation has been widely used in coastal ocean models because it is well-suited for varying bottom topography (Blumberg and Mellor 1987; Lynch and Werner 1987; Hadivogal et al. 1991). This transformation is no longer valid if the total depth D becomes zero. It seems difficult to incorporate a wet-dry point treatment program in the σ-transformation model because of this limitation. Two methods were proposed to avoid the occurrence of singular points when the local total water depth approaches zero in the area of dry points. The first method assumes that the currents vanish at dry points as a result of infinite horizontal and vertical diffusion. This approach is simple but it does not guarantee the volume conservation in numerical computation. The second method introduces an additional bottom boundary layer and redefines the local total water depth D as the sum of the local real depth [mean water depth H(x, y) + the surface elevation ζ(x, y, t)] and the thickness of the bottom boundary layer (h_c) (Ip et al. 1998). The grid is treated as a wet point if D is larger than h_c; otherwise it remains a dry point. In terms of physics, the bottom boundary layer is just like a viscous layer that is motionless. Technically, this layer should be sufficiently thin in order to satisfy a motionless condition and ensure numerical stability.

Adding a viscous layer at the bottom of the computational domain, we incorporated a 3-D wet-dry point treatment method into a 3-D, σ-transformation, primitive equations estuarine and coastal ocean model. The modified model was applied to a simulation of the temporal and spatial distributions of tidal currents and salinity in the Satilla River estuary. The water exchange process over the estuary-intertidal salt-marsh complex was examined based on the computed currents. A comparison of model results was made between the cases with and without inclusion of the flooding-drying process to estimate quantitatively the impact of this process on the water transport in the Satilla River estuary. The model results were also evaluated by direct comparison with observed tidal elevation, tidal currents, and salinity.

The Numerical Model and Experiment Design

The numerical model used in this study is the time-dependent, 3-D, primitive equations, estuarine and coastal circulation model (ECOM-si). This model was developed originally by Blumberg (1993) and modified by Chen and Beardsley (1998) and Zheng (1999) to add the 2-D and 3-D Lagrangian particle tracking programs. The model incorporates Mellor and Yamada's (1982) level 2.5 turbulent closure scheme to parameterize the vertical turbulent mixing and a free surface to simulate tidal wave propagation. A σ-coordinate transformation is used in the vertical to better represent the irregular bottom topography and an orthogonal curvilinear coordinate in the horizontal to properly fit the curvature of the shoreline. A semi-implicit numerical scheme is introduced for the time integration of the model, by which advection, Coriolis force, baroclinic pressure gradients, and horizontal diffusion terms are solved explicitly but the gradients of surface elevation are computed implicitly (Casulli 1990). A detailed description of the updated version of this model was given by Blumberg (1993) and the governing equations in the σ- and orthogonal curvilinear coordinates are briefly presented here.

Under the Boussinesq and hydrostatic approximations, the primitive momentum, salinity transport, and density equations were given as

$$\frac{\partial(h_1h_2Du)}{\partial t}+\frac{\partial(h_2Du^2)}{\partial\xi_1}+\frac{\partial(h_1Duv)}{\partial\xi_2}+h_1h_2\frac{\partial(\omega u)}{\partial\sigma}+Dv\left[-v\frac{\partial h_2}{\partial\xi_1}+u\frac{\partial h_1}{\partial\xi_2}-h_1h_2f\right]=-gDh_2\frac{\partial\zeta}{\partial\xi_1}-\frac{gD^2h_2}{\rho_0}\int_\sigma^0\left[\frac{\partial\rho}{\partial\xi_1}-\frac{\sigma}{D}\frac{\partial D}{\partial\xi_1}\frac{\partial\rho}{\partial\sigma}\right]d\sigma+\frac{h_1h_2}{D}\frac{\partial}{\partial\sigma}\left(K_m\frac{\partial u}{\partial\sigma}\right)+F_u \qquad (1)$$

$$\frac{\partial(h_1h_2Dv)}{\partial t}+\frac{\partial(h_2Duv)}{\partial\xi_1}+\frac{\partial(h_1Dv^2)}{\partial\xi_2}+h_1h_2\frac{\partial(\omega v)}{\partial\sigma}+Du\left[-u\frac{\partial h_1}{\partial\xi_2}+v\frac{\partial h_2}{\partial\xi_1}+h_1h_2f\right]=-gDh_1\frac{\partial\zeta}{\partial\xi_2}-\frac{gD^2h_1}{\rho_0}\int_\sigma^0\left[\frac{\partial\rho}{\partial\xi_2}-\frac{\sigma}{D}\frac{\partial D}{\partial\xi_2}\frac{\partial\rho}{\partial\sigma}\right]d\sigma+\frac{h_1h_2}{D}\frac{\partial}{\partial\sigma}\left(K_m\frac{\partial v}{\partial\sigma}\right)+F_v \qquad (2)$$

$$h_1h_2\frac{\partial\zeta}{\partial t}+\frac{\partial}{\partial\xi_1}\int_{-1}^0(uh_2D)\,d\sigma+\frac{\partial}{\partial\xi_2}\int_{-1}^0(vh_1D)\,d\sigma=0 \qquad (3)$$

$$\frac{\partial(h_1h_2DS)}{\partial t}+\frac{\partial(h_2DuS)}{\partial\xi_1}+\frac{\partial(h_1DvS)}{\partial\xi_2}+h_1h_2\frac{\partial(\omega S)}{\partial\sigma}=\frac{h_1h_2}{D}\frac{\partial}{\partial\sigma}\left(K_h\frac{\partial S}{\partial\sigma}\right)+F_S \qquad (4)$$

$$\rho_{total}=\rho_{total}(T_0,S)=\rho_0+\rho \qquad (5)$$

where ξ_1 and ξ_2 are the horizontal curvilinear orthogonal coordinates; u, v, and ω are the ξ_1, ξ_2, and σ velocity components, S is salinity, f is the Coriolis parameter, g is the gravitational acceleration, K_m is the vertical eddy viscosity coefficient, K_h is the thermal vertical eddy diffusivity, T_o is the reference temperature, ρ_0 is the reference density, ρ is the perturbation density, h_1 and h_2 are the metric factors of the coordinate transformation on the ξ_1 and ξ_2 axes, and $D = \zeta + H$ is the total water depth where ζ and H are the surface elevation and reference depth from $z = 0$, respectively. F_u, F_v, and F_S represent the horizontal momentum and thermal diffusion terms. To simplify the model calculations, the reference temperature is kept constant so that density is solely a function of salinity.

The true vertical velocity w on a σ surface is calculated by

$$w=\omega+\frac{1}{h_1h_2}\left[h_2u\left(\sigma\frac{\partial D}{\partial\xi_1}+\frac{\partial\sigma}{\partial\xi_1}\right)+h_1v\left(\sigma\frac{\partial D}{\partial\xi_2}+\frac{\partial\sigma}{\partial\xi_2}\right)\right]+\left(\sigma\frac{\partial D}{\partial t}+\frac{\partial\sigma}{\partial t}\right) \qquad (6)$$

The vertical eddy viscosity and diffusion coefficients are calculated using Mellor and Yamada's (1982) level 2.5 turbulent closure scheme, which include shear and buoyancy production of turbulent kinetic energy (TKE), TKE dissipation, TKE vertical diffusion, TKE advection, and temporal evolution of the TKE and turbulent macroscale.

The 3-D equations for q^2 and q^2l are given by

$$\frac{\partial(h_1h_2Dq^2)}{\partial t}+\frac{\partial(h_2Duq^2)}{\partial\xi_1}+\frac{\partial(h_1Dvq^2)}{\partial\xi_2}+h_1h_2\frac{\partial(\omega q^2)}{\partial\sigma}=2h_1h_2D(P_s+P_b-\varepsilon)+\frac{h_1h_2}{D}\frac{\partial}{\partial\sigma}\left(K_q\frac{\partial q^2}{\partial\sigma}\right)+F_{q^2} \qquad (7)$$

$$\frac{\partial(h_1h_2Dq^2l)}{\partial t}+\frac{\partial(h_2Duq^2l)}{\partial\xi_1}+\frac{\partial(h_1Dvq^2l)}{\partial\xi_2}+h_1h_2\frac{\partial(\omega q^2l)}{\partial\sigma}=1.8lh_1h_2D(P_s+P_b-0.56\varepsilon\hat{W})$$

$$+ \frac{h_1 h_2}{D}\frac{\partial}{\partial\sigma}\left(K_q \frac{\partial q^2 l}{\partial\sigma}\right) + F_l \qquad (8)$$

where $q^2 = (u'^2 + v'^2)/2$ is the TKE, l is the turbulent macroscale, K_q is the vertical eddy diffusion coefficient of the TKE, F_{q^2} and F_l represent the horizontal diffusion of the TKE and macroscale,

$$P_s = \frac{K_m}{D^2}\left[\left(\frac{\partial u}{\partial\sigma}\right)^2 + \left(\frac{\partial v}{\partial\sigma}\right)^2\right] \quad \text{and} \quad P_b = \frac{gK_h}{D\rho_0}\frac{\partial\rho}{\partial\sigma}$$

are the shear and buoyancy production terms of TKE, $\varepsilon = 0.06q^3/l$ is the TKE dissipation rate, $\hat{W} = 1 + 1.33l^2/(\kappa L)^2$ is a wall proximity function where $L^{-1} = (\zeta - z)^{-1} + (H + z)^{-1}$, and $\kappa = 0.4$ is the von Karman constant. In general, F_{q^2} and F_l are kept as small as possible to reduce the effects of horizontal diffusion on the solutions.

The TKE and macroscale equations are closed by defining

$$K_m = lqS_m, \qquad K_h = lqS_h, \qquad K_q = 0.2lq \quad (9)$$

where S_m and S_h are defined as the stability functions associated with

$$G_h = \frac{l^2 g}{q^2\rho_0 D}\frac{\partial\rho}{\partial\sigma}$$

(Galperin et al. 1988).

The surface and bottom boundary conditions for momentum and salinity are

$$\frac{\partial u}{\partial\sigma} = \frac{\partial v}{\partial\sigma} = 0; \qquad \frac{\partial S}{\partial\sigma} = 0;$$

$$\omega = 0, \qquad \text{at } \sigma = 0,$$

$$\frac{\rho_0 K_m}{D}\left(\frac{\partial u}{\partial\sigma}, \frac{\partial v}{\partial\sigma}\right) = (\tau_{bx}, \tau_{by}); \qquad \frac{\partial S}{\partial\sigma} = 0;$$

$$\omega = 0, \qquad \text{at } \sigma = -1, \quad (10)$$

where $(\tau_{bx}, \tau_{by}) = C_d\sqrt{u^2 + v^2}(u, v)$ are the ξ_1 and ξ_2 components of bottom stresses. The bottom drag coefficient C_d is determined by matching a logarithmic bottom layer to the model at a height z_{ab} above the bottom, i.e.,

$$C_d = \max\left[k^2/\ln\left(\frac{z_{ab}}{z_0}\right)^2, 0.0025\right] \qquad (11)$$

where z_o is the bottom roughness parameter, and z_{ab} is the height above the bottom of the first velocity (u,v) grid node.

The surface and bottom boundary conditions for the TKE and macroscale equations were given as

$$q^2 l = q^2 = 0 \qquad \text{at } z = \zeta, \quad \text{and}$$

$$q^2 l = 0, \qquad q^2 = B_1^{2/3}u_{\tau b}^2 \quad \text{at } z = -H \qquad (12)$$

where $u_{\tau b}$ is the friction velocity associated with bottom stresses and B_1 is an empirical constant equal to 16.6.

A 3-D wet-dry point treatment method is added to the ECOM-si in this study. To avoid the occurrence of singular points when the local total water depth approaches zero, we introduced a viscous layer with thickness of h_c into the model and redefined the local total water depth $D = H(x, y) + \zeta(x, y, t) + h_c$. If D is larger than h_c, the point is treated as a wet point and its velocity and elevation are computed from the finite difference equations. Otherwise it remains a dry point where water velocity is equal to zero. This approach is much like adding a porous medium with a thickness of h_c into the model (Ip et al. 1998). The advantages of this approach are its simplicity, conservative mass with no sacrifice of the σ-coordinator in making a perfect match of the irregular bottom topography, and arbitrary discretion resolution in the vertical. The thickness of the critical layer used in the Satilla River estuary model is 5 cm, which is determined based on sensitivity studies of velocity and tidal elevation to h_c. We also ran the model using $h_c = 1$ cm and found no significant difference between model results. This value is about 5 or more times smaller than that chosen by Ip et al. (1998) in their 2-D model experiments in Great Bay, New Hampshire (in their experiments, $h_c = 25$ cm).

The original ECOM-si code incorporates a central difference scheme for the calculation of the nonlinear advection terms. This scheme fails to simulate the tracer field when the flooding-drying process is included over the intertidal zone. For this reason, we used the Multidimensional Positive Definite Advection Transport Algorithm (MPDATA) introduced by Smolarkiewicz (1984) to solve nonlinear advection terms in salinity transport Eq. 4. This scheme uses the anti-diffusion velocity to the successive application of an upwind scheme with correction to the first-order truncation error. This procedure, when repeated, yields a positive definite and second-order accurate advection algorithm. This algorithm was successfully applied to the study of the frontward transport of nutrients on Georges Bank (Chen and Beardsley 1998). We simply adapted the well-tested MPDATA subroutine from Chen and Beardsley (1998)'s Georges Bank model to the Satilla River estuary model.

A particle-tracking program was incorporated into the ECOM-si by Chen and Beardsley (1998) and it was subsequently modified by Zheng (1999). In this program, particle trajectories are traced by solving the x, y, and σ velocity equations

$$\frac{dx}{dt} = u, \qquad \frac{dy}{dt} = v, \quad \text{and} \quad \frac{d\sigma}{dt} = \frac{\omega}{h + \varsigma} \qquad (13)$$

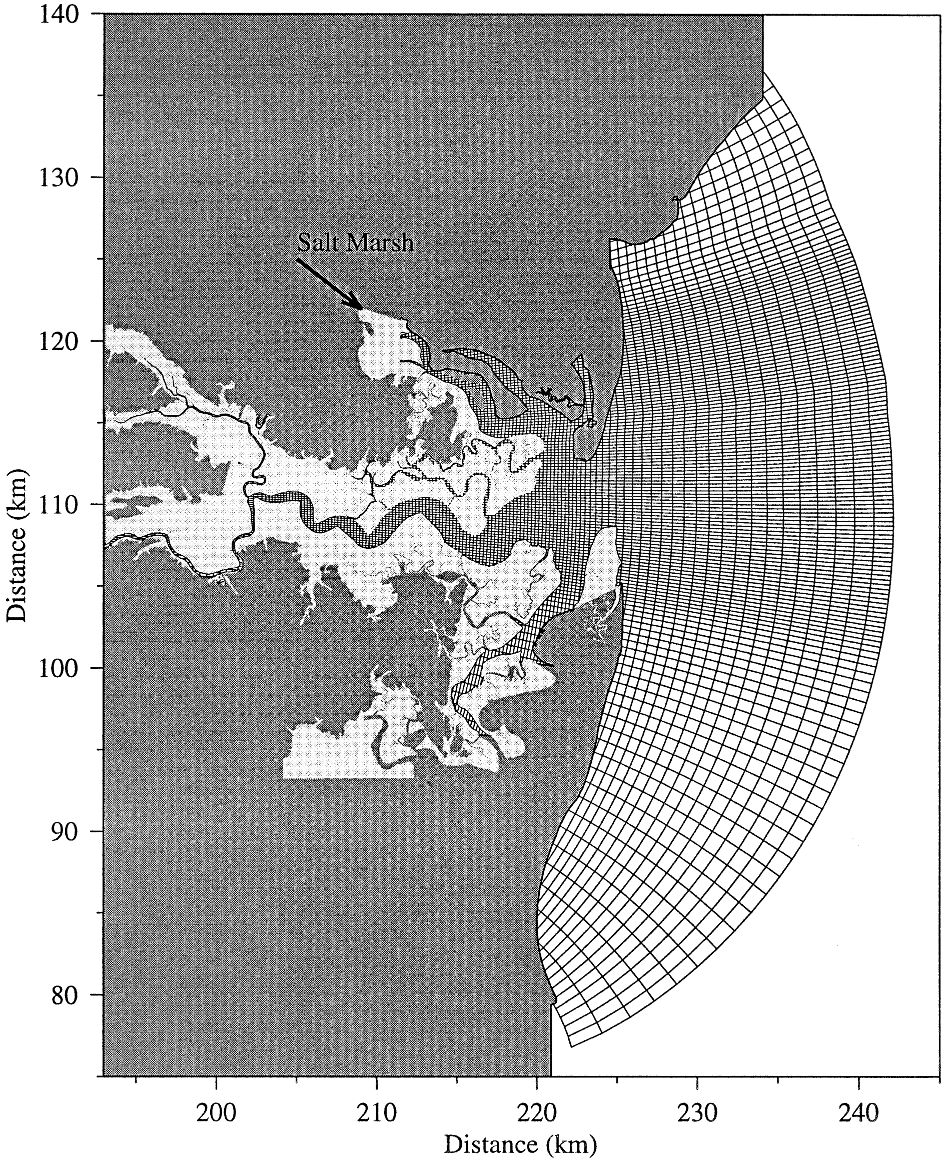

Fig. 2. The numerical computational grid. The gray-filled area is the 2-m intertidal zone that can be reached during a flood tidal period. The numerical domain consists of 148 (along-river) × 141 (cross-river) × 11 (vertical) grid points. The horizontal resolution is 100 m in the main river channel and intertidal zone and gradually increases to 2.5 km over the inner shelf.

where u, v, and ω are the x, y, and σ components of particle velocity, respectively. The kinematic equations for u, v, and ω are calculated using a fourth-order Runge-Kuta integration method with a truncation error of the order $(\Delta t)^5$. The particle velocity is determined by a bilinear interpolation from the eight nearest grid points. At each time step, each particle is checked to determine whether it is located inside the model domain. If a particle moves out of the numerical domain, it is no longer tracked. The time step Δt is chosen to satisfy the criterion $\Delta t \cdot K < 0.05$, where K is an upper bounding of the spatial gradient of velocity. The particles are tracked in the model space (x, y, σ) and then their trajectories are converted to physical space (x, y, z). This method avoids interpolation errors due to repeated transformation from the σ-coordinate and the z-coordinate.

The model domain covers the entire Satilla River estuarine area with an outer boundary at 2-m elevation lines and an open boundary at the inner shelf of the South Atlantic Bight (SAB), 20 km away from the river mouth (Fig. 2). The horizontal grids are designed using an orthogonal curvilinear coordinate with a total of 148 (along-river) × 141 (cross-river) points. The horizontal resolution is

100 m in the main estuarine channel and intertidal zones and it increases gradually to 2.5 km in the inner shelf. The large grid sizes chosen near the open boundary are used to numerically filter the short internal waves reflected back to the boundary. This has been demonstrable to be an efficient way to ensure the stability of numerical computation with open boundaries (Chen and Beardsley 1995; Chen et al. 1995). Eleven σ-levels are used in the vertical that correspond to a vertical resolution of less than 2.2 m at the 23-m depth (the deepest depth of the computational domain) and 0.2 to 0.5 m in the main estuarine channel. The time step in all the model runs is 41.4 s, 1,080 time steps over an M_2 tidal cycle.

The model is initially driven by the M_2, S_2, and N_2 tidal elevations and phases at the open boundary in the inner shelf. The amplitudes and phases of the M_2, S_2, and N_2 tidal forcing are specified directly using the output of Chen et al. (1999)'s SAB inner shelf tidal model. A gravity wave radiation boundary condition with a propagation speed of $\sqrt{gh}$ is specified at the open boundary for the current, which allows the reflected tidal energy to radiate out of the numerical domain (Chen and Beardsley 1995). To avoid the numerical instability caused by a sharp change in initial conditions, the tidal forcing is ramped up from zero to its full value over one M_2 tidal cycle. To focus on the physical interaction processes associated with freshwater discharges and tides, the temperature is simply specified as constant throughout the computational domain. Freshwater is injected into the model domain at the upstream end of the estuary as a volume flux as

$$V_0 = \sum_{i=1}^{N} \left[D(i) \int_{-1}^{0} v_o(i, \sigma)\, d\sigma \right] \Delta l(i) \qquad (14)$$

where v_o is the velocity normal to the coastline, and N is the total grid points for freshwater input, and $\Delta l(i)$ is the width of the cell i.

Numerical experiments reported in this paper are conducted for three cases. In the first case, the model is driven only by tidal forcings in which temperature and salinity are specified as constant (20 and 35 psu) everywhere with inclusion of the intertidal salt marsh zone. The second case is the same as the first case but excludes the intertidal salt-marsh zone. In the third case, the model was driven by tides plus real-time freshwater discharge under the observed initial salinity field. The model is initialized using the salinity data obtained from the conductivity-temperature-depth (CTD) measurement on April 7, 1995 (at the neap tide), and was run for 9 consecutive days. Then the model results are compared with the observations taken on April 15, 1995 (at the spring tide).

The Tidal and Salinity Simulation

The Tidal Simulation

To resolve the spring-neap tidal cycle, the model was run for 40 d (about 80 M_2 tidal cycles). The M_2, S_2, N_2, and other tidal constituents were separated from the model-predicted surface elevation and current data using Foreman's (1978) tidal harmonic analysis program. A direct comparison between model-predicted and observed amplitudes and phases of tidal constituents was made at the 5 bottom pressure measurement sites shown in Fig. 1. The model simulated the spring and neap tidal variations in the main channel of the river and the flooding-drying process over the intertidal zone.

The flooding-drying process can be viewed clearly from the snapshot distribution of the near-surface tidal current vectors at different phases of a dominant M_2 tidal period (Fig. 3). A phase delay was clearly evident at the transition from ebb to flood tide. The tidal current was inward near the mouth of the estuary but it still remained outward in the upstream area. The maximum phase delay between the two ends of the estuary was about 1 h, which was in reasonable agreement with the estimated phase difference of 47 min found in the October 26, 1995, Land-Margin Ecosystem Research survey (spring tide) along the Satilla River estuary. This along-estuary phase difference was believed to be a result of the along-estuarine variation of bottom friction, which increased inward as the water became shallower.

In the flood tidal phase, the tidal current was strongest in the main channel of the river, decreased inward and toward the salt marsh. The velocity at the edge between the river channel and salt marsh could reach 80 cm s^{-1}, about 60% of the maximum tidal velocity found in the main channel. About the 80% to 90% of the salt-marsh area was covered by water at the maximum flood tide.

When tidal currents reversed to ebb tide, a remarkable divergence and convergence occurred in the along-estuary direction. The water moved outward near the mouth of the river at a speed of 20 cm s^{-1}, but it still flowed inward farther upstream at a speed of about 50 cm s^{-1}. At the maximum ebb tide, the outward current was strongest inside the estuary and the maximum speed reached 150 cm s^{-1} near the mouth of the river. This speed was about 10% to 20% greater than that found at the maximum flood tide. At this time, about 80% of the water over the salt marsh had drained back into the main channel of the river.

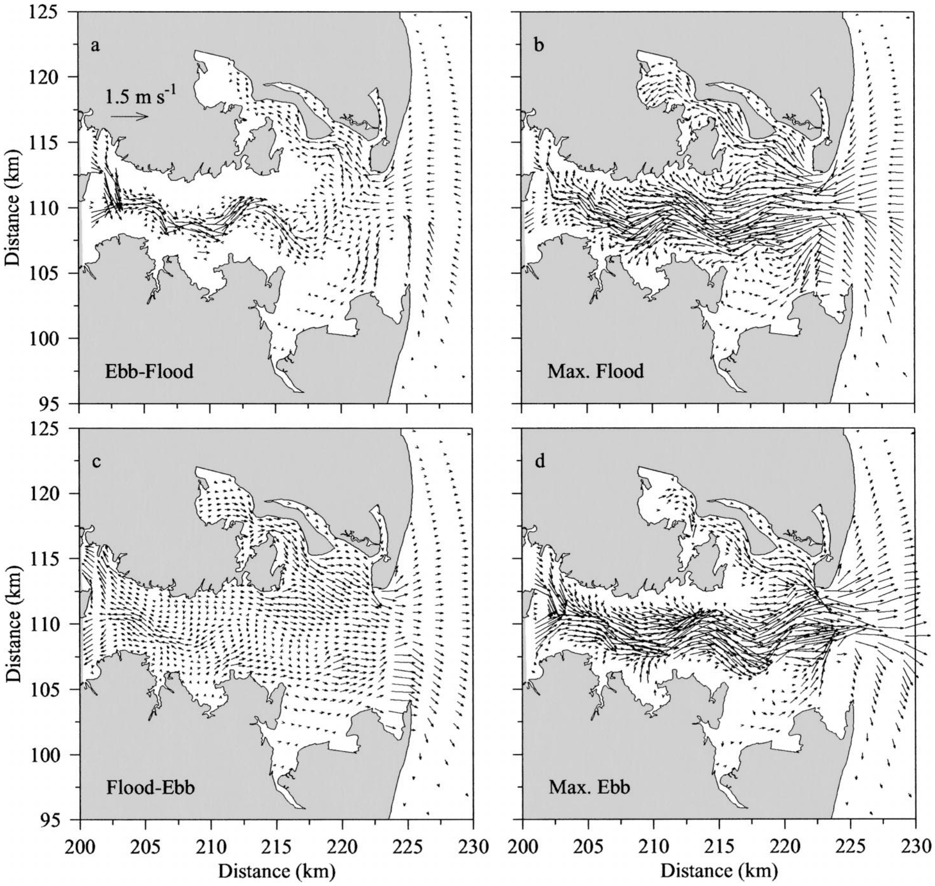

Fig. 3. Synoptic distributions of the near-surface tidal current vectors at the transition from ebb to flood (a), the maximum flood (b), the transition from flood to ebb (c), and the maximum ebb (d) for the case with inclusion of the flooding-drying process.

The model-predicted tidal elevation and currents were compared directly to the hourly tidal heights and currents observed at 5 bottom pressure measurement stations and two current meter sites, respectively (Figs. 4 and 5). The tidal height measurements were made from January 23 to March 13, 1999, using the Sea-Bird Electronics SEACAT data logger. Foreman's (1978) tidal harmonic analysis program was used to construct the amplitudes and phases of the major tidal constituents from the tidal height data (Table 1). The data showed that the amplitude of M_2 increased inward gradually from 94.7 cm at site 1 to 99.4 cm at site 4 and then decreased to 96.0 cm at site 5 near the estuary's upstream end. The phase of the M_2 tidal constituent increased inward, with a time delay of 57 min between site 1 and site 5. The along estuary distributions of the amplitudes and phases of the S_2 and N_2 tidal constituents had the same trend. Amplitudes increased slightly from 17.9 and 17.6 cm at site 1 to 18.3 and 17.9 cm at site 2 and then decreased gradually to 16.6 and 16.9 cm at site 5, respectively. Phases increased inward from 51.7° and 11.1° at site 1 to 91.8° and 51.8° at site 5, respectively. The phase lag difference between the estuary's mouth and head was about 1.5 h for both S_2 and N_2 tidal constituents. The M_4 tidal constituent, which was caused by the distortion of the M_2 tide, was one order of magnitude smaller than the M_2 tide in the Satilla River estuary. The amplitude of this tidal constituent increased inward from 2 cm at site 1 to 7 cm at site 5, and its phase decreased from 323.7° at site 1 to 316.1° at site 2 and then increased to 351.4° at site 5.

To examine how the tidal simulation was affected by the flooding-drying process over the intertidal zone in the Satilla River estuary, we conducted two types of numerical experiments with and without inclusion of the flooding-drying process. In the case with inclusion of the flooding-drying process, the model showed a reasonable simulation regarding good agreement in along-estuarine trends, amplitudes, and phases between the model-predicted and observed values of the M_2, S_2, and N_2 tidal constituents (Fig. 4, Table 1). The maximum mod-

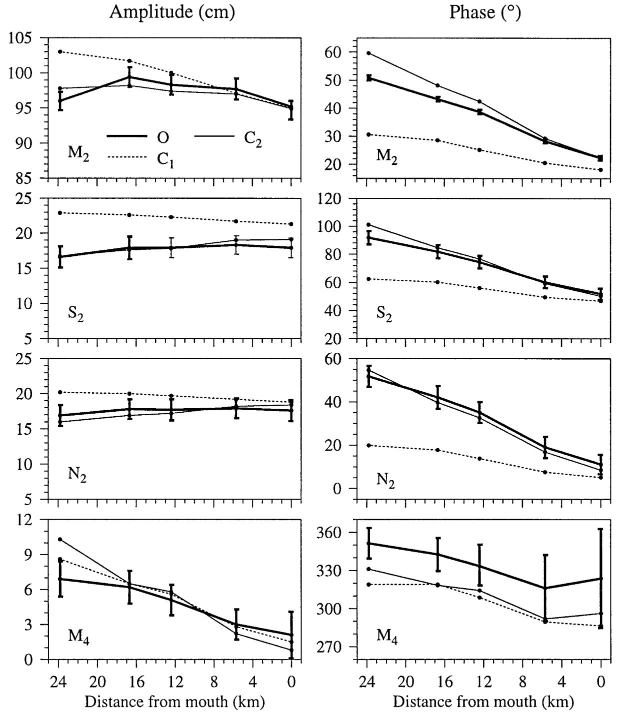

Fig. 4. Comparisons of measured and model-predicted M_2, S_2, N_2, and M_4 tidal amplitudes (left panel) and phases (right panel) at along-estuary transects shown in Fig. 1. The error bars are sample standard deviation at a 95% confidence level. O = observation; C_1 is for the case without inclusion of flooding-drying process; and C_2 is for the case with inclusion of flooding-drying process.

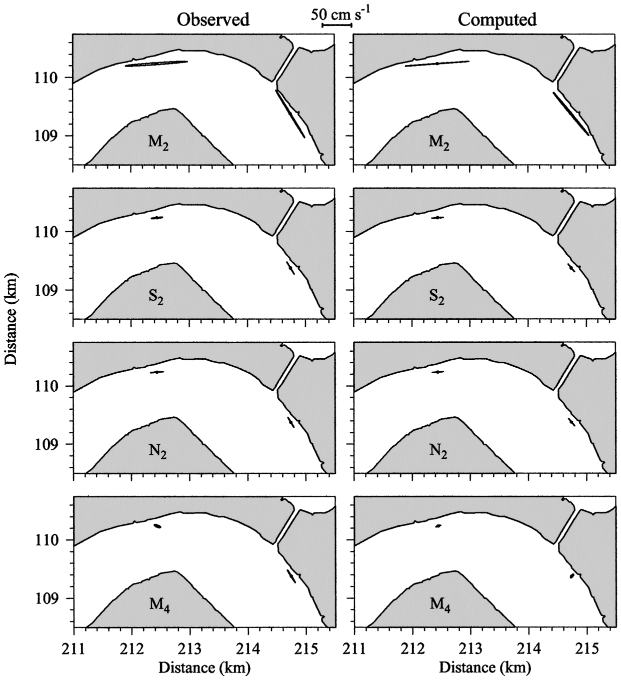

Fig. 5. Comparisons of measured (left panel) and model-predicted (right panel) M_2, S_2, N_2, and M_4 tidal current ellipses at two current meter mooring sites (A and E). The model-predicted tidal currents shown here are for the case that includes the flooding-drying process.

el-data water level differences in amplitude and phase were 1.8 cm and 8.8° for the M_2 tide, 1.2 cm and 9.3° for the S_2 tide, and 0.9 cm and 3.9° for the N_2 tide. The model also reasonably simulated the elevation of the M_4 tidal constituent regarding

TABLE 1. Observed and computed tidal amplitudes and phases of M_2, S_2, N_2, and M_4 tides at the 5 along-estuary sites for January 20–March 19, 1999. O = observation; C_1 is without inclusion of flooding-drying process; C_2 is with inclusion of flooding-drying process.

		Amplitude (cm)			Phase (degree)		
		O	C_1	C_2	O	C_1	C_2
M_2	Site 1	94.7 (1.3)	95.0	94.9	22.3 (0.8)	18.1	22.4
	Site 2	97.7 (1.5)	97.1	97.0	28.3 (0.7)	20.5	29.3
	Site 3	98.3 (1.4)	100.0	97.4	38.7 (0.8)	25.2	42.4
	Site 4	99.4 (1.4)	101.7	98.2	43.2 (0.8)	28.6	48.1
	Site 5	96.0 (1.3)	103.0	97.8	50.8 (0.9)	30.6	59.6
S_2	Site 1	17.9 (1.4)	21.3	19.1	51.7 (4.0)	46.7	50.1
	Site 2	18.3 (1.3)	21.7	19.0	60.1 (4.1)	49.4	59.2
	Site 3	17.9 (1.4)	22.3	17.8	74.4 (4.4)	56.0	76.7
	Site 4	17.9 (1.6)	22.6	17.6	81.8 (4.7)	60.2	84.6
	Site 5	16.6 (1.5)	22.9	16.7	91.8 (4.8)	62.5	101.1
N_2	Site 1	17.6 (1.5)	18.8	18.4	11.1 (4.5)	5.1	8.5
	Site 2	17.9 (1.4)	19.2	18.2	19.0 (4.9)	7.6	16.8
	Site 3	17.7 (1.5)	19.7	17.2	35.1 (4.8)	13.8	32.6
	Site 4	17.8 (1.4)	20.0	16.9	42.1 (5.3)	17.7	39.7
	Site 5	16.9 (1.5)	20.2	16.0	51.8 (4.8)	19.9	54.7
M_4	Site 1	2.1 (2.0)	1.4	0.8	323.7 (39)	285.9	296.3
	Site 2	3.0 (1.3)	2.6	2.2	316.1 (26)	290.6	292.0
	Site 3	5.1 (1.3)	5.1	5.8	334.3 (16)	310.1	314.3
	Site 4	6.2 (1.4)	6.7	6.5	342.6 (13)	319.1	318.3
	Site 5	6.9 (1.5)	7.8	10.3	351.4 (12)	320.6	331.1

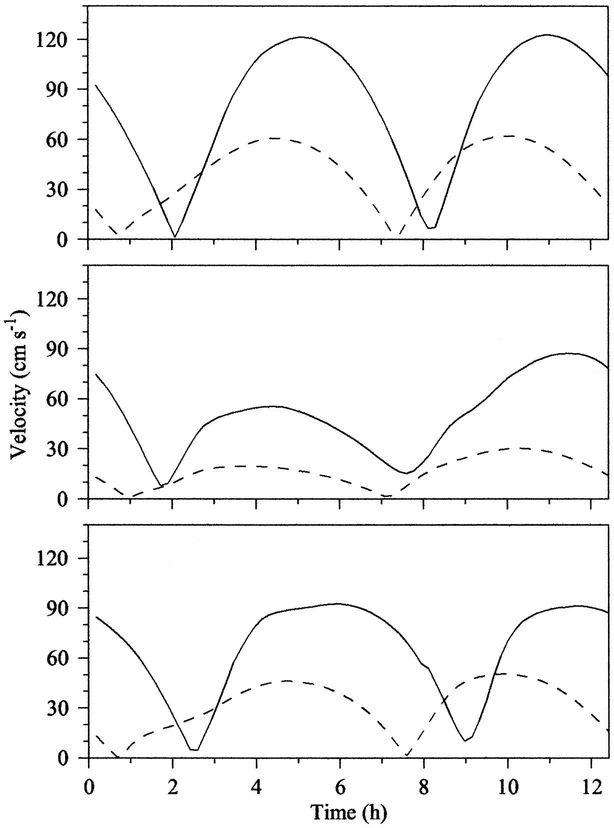

Fig. 6. Comparisons of the near-surface tidal current speed over an M_2 tidal cycle at the three selected sites for the cases with (solid line) and without (dashed line) inclusion of the flooding-drying process. Three selected sites are located at river mouth (upper), 2.5 km upstream from the river mouth (middle), and 12 km upstream from the river mouth (lower).

the inward increased trends in both amplitude and phase. The phase difference between model-predicted and observed M_4 tidal elevations was about 0.5 h at site 5 close to the upstream end of the river.

The model-predicted current ellipses of the M_2, S_2, N_2, and M_4 tides also were in good agreement with observed current ellipses at mooring sites A and E (see Fig. 1 for locations of these two sites). The maximum differences in major axes, orientations, and phases were less than 2 cm s^{-1}, 9°, and 7 min for M_2 tide; 4 cm s^{-1}, 9°, and 25 min for S_2 tide; and 2 cm s^{-1}, 9°, and 25 min for N_2 tide, respectively (Table 2). The tidal current simulation seemed much better at site A than at site E. A relatively large model-data difference in orientation at site E was likely due to the discrepancy between the model and realistic depths at that site and failure to resolve a small tidal creek in the tidal simulation. This was consistent with a poor simulation for M_4 at site E, since this tidal constituent was mainly produced by the nonlinear interaction of tidal currents over bottom topography.

Ignoring the flooding-drying process over the intertidal zone resulted in the overestimation of amplitude and underestimation of phase for the M_2, S_2, and N_2 tidal elevations. The model showed a faster inward increase of the amplitude of the M_2 tide. At site 5, the model-predicted amplitude was about 7 cm higher than the observed amplitude. Although the inward trends of the model-predicted and observed M_2 tidal phases were similar, their difference increased inward and at site 5 the model-predicted phase was 20° smaller than the observed phase. Similar differences also were found for the S_2 and N_2 tidal constituents, implying that ignoring the flooding-drying process not only enlarges the amplitude of tidal waves upstream but also makes the inward propagation of tidal waves faster.

A significant underestimation was found in tidal currents when the flooding-drying process was removed (Table 2). At site A, for example, the major axis of the M_2 tidal current ellipse was 54.7 cm s^{-1} in the case with inclusion of the flooding-drying

TABLE 2. Comparison of Md_2, S_2, N_2, and M_4 tidal current parameters between observed and computed tidal currents at two mooring stations A and E. Site A was located at 81°32.28′W, 30°59.58′N and site E was at 81°30.84′W, 30°59.16′N. The current record was measured March 26–April 27, 1999. O = observation; C_1 is without inclusion of flooding-drying process; C_2 is with inclusion of flooding-drying process. U_{major} = amplitude of the major axis; U_{minor} = amplitude of the minor axis; θ_{orien} = orientation of the major axis; G = time of maximum current (Greenwich phase in degree, 1° = 2.07 min for M_2 tide). The orientation was measured counterclockwise from the east. The positive sign in U_{minor} indicated a counterclockwise rotation of current vectors.

		U_{major} (cm s^{-1})			U_{minor} (cm s^{-1})			θ_{orien} (°)			G (°)		
		O	C_1	C_2	O	C_1	C_2	O	C_1	C_2	O	C_1	C_2
Site A	M_2	53.4 (0.77)	19.3	54.7	−1.6 (0.47)	−0.2	−0.2	4.2 (0.5)	7.7	4.3	156.7 (0.8)	118.5	154.6
	S_2	9.6 (0.78)	4.6	10.1	−0.6 (0.51)	−0.02	−0.2	5.2 (3.6)	73	3.8	203.0 (4.7)	150.8	189.6
	N_2	11.0 (0.88)	3.8	9.3	−0.3 (0.47)	−0.01	−0.1	4.3 (2.6)	7.4	4.0	142.4 (4.1)	108.3	144.6
	M_4	5.7 (0.77)	3.8	4.3	1.6 (0.42)	0.2	0.8	157.3 (6.4)	12.3	200.9	190.5 (7.9)	197.9	186.3
Site E	M_2	47.8 (0.95)	26.4	47.6	0.8 (0.40)	0.2	1.2	121.3 (0.5)	126.4	129.6	150.0 (1.2)	116.3	151.3
	S_2	12.6 (1.02)	6.3	8.8	−0.1 (0.44)	−0.1	−0.2	121.2 (2.1)	125.1	130.2	16.4 (5.0)	328.8	5.0
	N_2	10.0 (0.94)	5.2	8.1	0.2 (0.42)	0.1	0.2	120.7 (2.6)	125.2	129.8	309.0 (5.9)	287.1	321.0
	M_4	12.6 (0.76)	4.7	3.9	0.5 (0.40)	0.3	1.3	121.9 (2.1)	123.6	54.2	167.3 (4.2)	190.0	195.0

process. In the case without inclusion of the flooding-drying process it dropped to 19.3 cm s^{-1}, a reduction of about 60%. A similar difference was reported at site E where the magnitude of the M_2 tidal current was reduced by about 45% when the flooding-drying process was removed. Ignoring the flooding-drying process not only failed to simulate the amplitude of tidal currents but also caused a shift of their phases. The time at which the maximum current was reached was about 1 h earlier compared with the case that included the flooding-drying process (Fig. 6). These differences also were true for the S_2 and N_2 tidal currents, indicating that the flooding-drying process must be taken into consideration in order to simulate the tidal current in the Satilla River.

THE SIMULATION OF SALINITY

The tidal simulation indicates that the flooding-drying process over the intertidal zone must be included in order to simulate water transport in the Satilla River estuary. For this reason, we have conducted the salinity simulation only for the case that includes tidal flushing-draining over the intertidal zone. Numerical experiments were carried out in two steps. First, the model was run only with tidal forcings for about 30 d. When tidal currents and elevations of M_2, S_2, and N_2 tidal constituents reached an equilibrium state, all the variables at SLW during neap tide were output and saved as a restart file. The model was re-run with initial conditions of the salinity field taken along the estuary on April 7, 1995, and the flow field specified from the restart file. The model-predicted salinity output from the eighth day was compared instantaneously to the real-time salinity measured on an along-river transect on April 15, 1995, (during spring tide). The model-predicted salinity also was compared instantaneously with salinity taken over an M_2 tidal cycle at an anchor site shown in Fig. 1. To examine how the spring tide-induced stronger tidal mixing and advection affect the spatial and temporal distributions of salinity in the estuary, we ran the model with the same salinity and freshwater discharge conditions under the flow environment with the only M_2 tidal forcing. The freshwater discharge rate was obtained from the U.S. Geological Survey gauge station and adjusted for ungauged area by Alber and Sheldon (1999). The discharge was highest on April 7 (166 m^3 s^{-1}) and lowest on April 16 (113 m^3 s^{-1}).

The model predicted a reasonable synoptic distribution of surface salinity in the Satilla River estuary (Fig. 7). During the flood tidal phase, the tidal current advected the higher salinity water into the estuary, resulting in a relatively large along-estuary salinity gradient inside the estuary. During the ebb tidal phase, the combined gravitational and tidal flows moved the low salinity water seaward from the upstream, leading to a rapid decrease of salinity in the estuary and near the mouth of the estuary. The salinity change over one M_2 tidal cycle was 9 psu near the estuarine mouth and reached a maximum value of 12 psu at a place 16 km upstream.

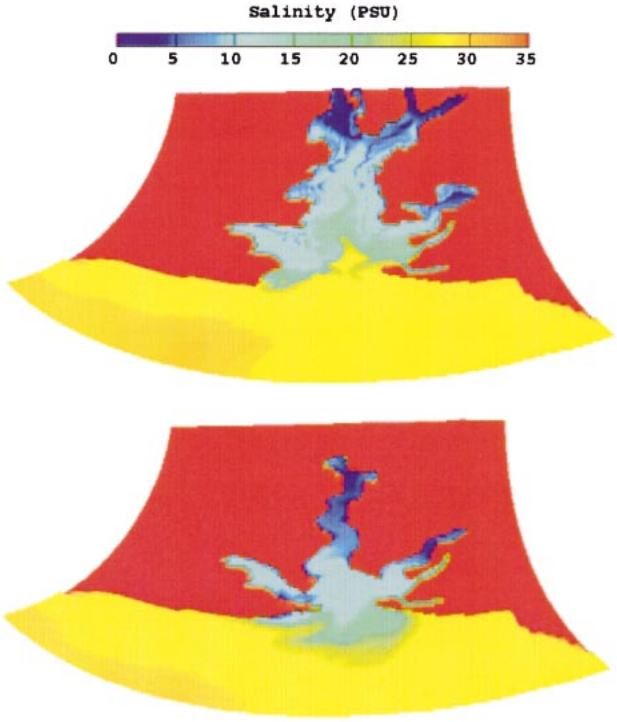

Fig. 7. A 3-D view of the synoptic distribution of model-predicted, near-surface salinity at slack high water (SHW: upper) and slack low water (SLW: lower) on April 15, 1995, for the experiment with inclusion of the flooding-drying process.

The location of the largest along-estuary salinity gradient varied with tidal cycle over a variation scale of about 12 km. At SLW, it was located at a place about 4 km upstream of the estuary's mouth with an along-estuary salinity gradient of 2 psu km^{-1}. At SHW, it migrated inward to a place about 16 km upstream of the estuary's mouth where the along-estuary salinity gradient increased to 5 psu km^{-1}. The larger along-river salinity gradient found in the flood tide was mainly due to the cancellation between buoyancy-induced and tidal current during that period.

Good agreement was found in the along-river distribution of salinity between model results and observations (Fig. 8a,b). The observation showed a well-mixed distribution of salinity along the river, with a range from 26 psu near the river mouth to 3 psu near the upstream end of the main river channel. There was clear evidence of the intrusion

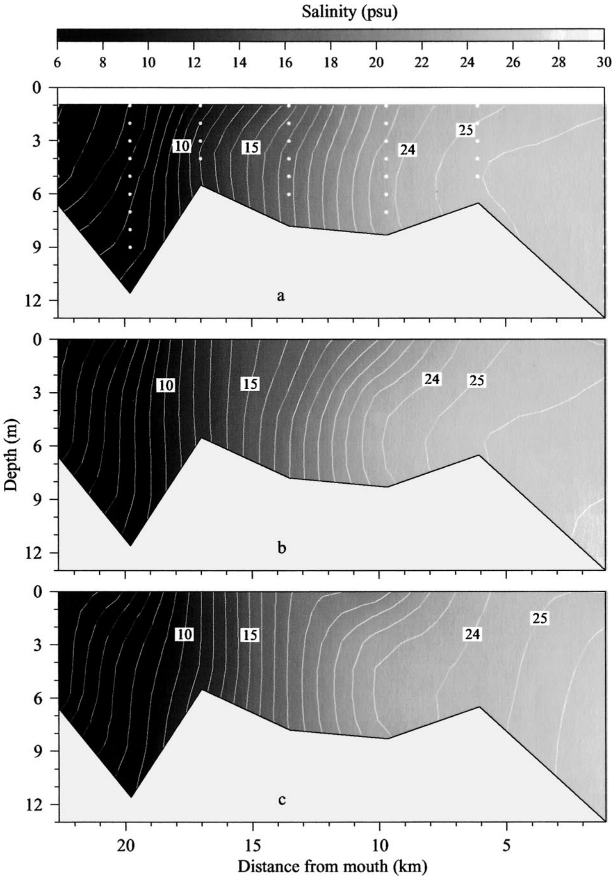

Fig. 8. Comparison of the observed and model-predicted spatial distributions of salinity on an along-river CTD transect. a) observations, b) M_2, S_2, and N_2 tides plus river discharge, and c) M_2 tide plus river discharge. The observation was conducted on April 15, 1995, during spring tide. The model was initialized using the CTD data taken on April 7, 1995, and run for 8 additional days until April 15, 1995. Dots in the upper panel represents the measurement locations.

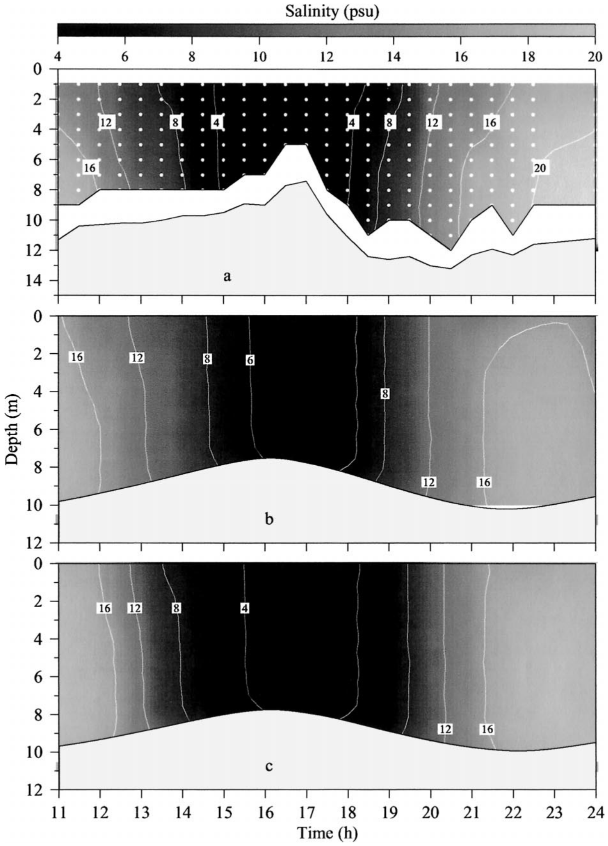

Fig. 9. Comparison of the observed and model-predicted temporal distributions of salinity at an anchor site C. a) observations, b) M_2, S_2, and N_2 tides plus river discharge, and c) M_2 tide plus river discharge. During the measurement, the surface was selected as the origin of the coordinate ($z = 0$). The shadow area indicates the temporal variation of sea elevation rather than real bottom topography. Dots in the upper panel represents the measurement locations.

of oceanic water around mid-depth near the river mouth, where a significant curvature was found in the salinity contour of 26 or higher. These observed features were well captured in the model simulation, except for a slightly higher along-river gradient of salinity near the upstream end of the main river channel.

The model-data comparison of the temporal distribution of salinity at the anchor site also was reasonable (Fig. 9a,b). Observed salinity at that site exhibited a significant time variation over an M_2 tidal cycle: 15 psu at SHW, less than 4 psu at SLW, and 20 psu at the next SHW. The water was vertically well-mixed at SLW and slightly stratified at SHW (Blanton et al. 1999). The model-predicted salinity was in reasonable agreement with observed salinity regarding the occurrence time of the lowest salinity and vertically well-mixed structures. The model-predicted lowest salinity was about 1 psu higher than observed salinities. This discrepancy might be caused by factors associated with differences between the model grid and the observation location, and other freshwater resources, such as groundwater input (Moore 1996), freshwater sources in the salt-marsh zone, and local precipitation. At these factors were ignored in our model experiment.

Ignoring the S_2 and N_2 tidal constituents in the model simulation failed to resolve the spring-neap tidal cycle in the Satilla River estuary. In this case (with the M_2 tidal forcing only), the model results showed a 1-km outward shift in the location of the salinity contour, even though the model-predicted and observed overall structures of the salinity were in reasonable agreement (Figs. 8c and 9c). The intrusion of oceanic water around mid-depth near the river mouth also disappeared. These data-model disparities were caused by a failure to resolve the spring-neap tidal variation. This variation accounted for a 15% increase in both tidal currents and vertical mixing. It is interesting to note here that the increased vertical mixing, which is due to the spring tides, had little influence on the vertical structure of salinity. When compared to the increase in spring tide-induced vertical mixing, the spring tide-induced horizontal advection increase was overwhelming during that period. These results were consistent with previous observations and model studies in the estuary and inner shelf of the SAB (Blanton 1996; Chen et al. 1999).

It should be pointed out that the models predicted more symmetrical salinity over one tidal cycle and failed to simulate the high salinity value of 20 psu at the second SHW on April 16, 1995. The unusually high salinity observed at the anchor site was probably the result of wind-driven salt intrusion. The meteorological measurements taken near the Satilla River estuary on April 16, 1995, showed a northward wind from 1100 to 2100 that then rotated clockwise to northeast. The wind speed was 0.5 to 1 m s^{-1}. The along-shelf component of the northward or northeastward winds tended to cause an outward transport from the estuary to the inner shelf near the surface and strengthened estuarine gravitational circulation. This in turn caused oceanic higher salinity water near the bottom to intrude into the estuary.

THE RESIDUAL FLOW FIELD

The residual flow in the Satilla River estuary was mainly driven by tidal and topographic interaction, turbulent mixing, and buoyancy forcing. The residual currents described below were the subtidal flows that were separated from tidal currents using Foreman's harmonic analysis program. Three experiments were conducted: the M_2 tide only, the M_2 plus S_2 and N_2 tides, and the M_2, S_2, and N_2 tides plus river discharge. For the experiment with the M_2 tide only, the model-predicted near-surface residual flow field in the main channel of the river is characterized by multiple eddy-like convergences and divergences (Fig. 10a). In the inner shelf, the model shows two eddy-like circulations: cyclonic in the northern part and anticyclonic in the southern part. A strong outflow is found in the main channel, 3 km upstream from the mouth of the estuary. This flow splits northeastward and southeastward near the estuarine mouth, forming a saddle area in the shallowest area. The northeastward flow moves into the northern branch of the estuary to form an anticyclonic eddy-like circulation there, while the southeastward flow leads to a convergence in the southern branch of the estuary. The residual current is about 38 cm s^{-1} in the upstream area, 5 km inward from the estuarine mouth, 25 cm s^{-1} at edge of the main estuarine channel and salt marsh, and 2–20 cm s^{-1} in the inner shelf.

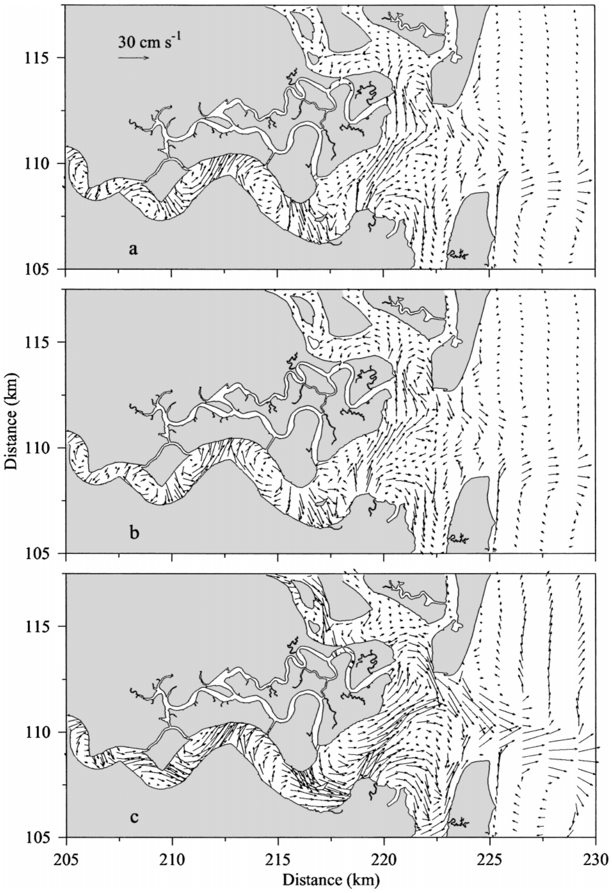

Fig. 10. Synoptic distributions of near-surface residual current vectors for the cases with M_2 tidal forcing only (a); M_2, S_2, and N_2 tidal forcing (b); and M_2, S_2, and N_2 tides plus river discharge (c).

Adding the spring-neap tidal cycle had little influence on the spatial distribution of the residual flow (Fig. 10b). The current in most areas inside the river remains almost the same for both the cases with the M_2 tide only and the M_2 plus S_2 and N_2 tides, except in the upstream area, 10 km inward from the river mouth. The eddy-like residual circulation is slightly stronger when the spring-neap tidal cycle is included.

The near-surface residual flow intensifies significantly when freshwater discharge is added (Fig. 10c). Although the spatial distribution of the residual circulation is very similar to that in the case with tidal forcings only, the residual current is about 5 to 15 cm s^{-1} stronger. This suggests that the along-estuarine baroclinic pressure gradient plays a significant role in estuarine circulation in the Satilla River estuary. A relatively stronger northward residual flow occurs in the southern branch of the estuary, which enhances significantly a near-surface convergence at the middle point of the branch. The offshore flow in the inner shelf increases to 30 cm s^{-1}, which remarkably intensifies the anticyclonic residual circulation on the southern coast of the estuary.

The model-predicted tidal residual flow field is characterized by multiple eddy-like convergences and divergences. The clockwise-counterclockwise eddies outside the inlet were found in model studies (Imasato 1983; Kapolnai et al. 1996; Wheless and Valle-Levinson 1996) and in observations (Candwick and Largier 1999) of other estuaries. These complex residual circulation patterns were significantly intensified by river discharge, and the field pattern tends to migrate downstream under the buoyancy condition.

The model also shows that the locations of the eddy-like residual circulation are closely related to local geometry, suggesting that topographic tidal rectification probably was one of the important physical driving mechanisms responsible for the existence of these complex residual flow patterns. The theory of tidal rectification over a variable bottom topography has been well explored in coastal and shelf regions (Huthnance 1973; Zimmerman 1978; Loder 1980; Chen and Beardsley 1995; Chen et al. 1995). Research shows that tidally rectified flow generally flows around the variable bottom slope with the shallow side on its right. Some of the residual circulation patterns found in the Satilla River estuary were consistent with this theory but other patterns were completely opposite. This implies that additional physical processes must be taken into consideration in order to interpret the formation of multiple eddy-like residual circulations in an estuary like the Satilla River.

The bent coastline and the asymmetry of tidal currents seemed to play important roles in the formation of the complex residual circulation patterns in the Satilla River estuary. In a curved estuarine channel, the imbalance between the centripetal and cross-estuary pressure gradients would directly contribute to the intensification of residual flow around the curved estuarine channel (Fischer et al. 1979; Geyer 1993; Ridd et al. 1998). This was consistent with the spatial distribution of the residual flow found in the Satilla River estuary, where the largest convergence and divergences occurred at the place where the maximum curvature of the coastline was located. The existence of intertidal salt mashes significantly enhanced tidal asymmetry between flood and ebb tides, and hence caused significant tidal residual flow in the estuary. Such an asymmetry became much more significant when freshwater discharge was included. All of this evidence suggests that the complex residual flow field in the Satilla River estuary was caused by topographic tidal rectification with the superimposition of inertial effects of coastal curvature, flooding-drying processes, freshwater discharge, and an along-river baroclinic pressure gradient.

The Salt Marsh-Estuary-Shelf Water Exchanges

One of the most important issues in the study of estuarine ecosystems is simulating the water transport associated with the flooding-draining process over the intertidal salt marsh-estuary-shelf complex. Since the water exchange in such a tidal system follows the kinematics associated with the Lagrangian theory, no water or nutrient transport could be estimated without understanding the nature of fluid particle trajectories. Several basic questions have not been examined in the Satilla River estuary. Is the water exchange process over the intertidal salt marsh-estuary similar on the northern and southern sides of the river? Could there be an exchange of water across the river between the northern and southern salt-marsh areas? How are fluid particle trajectories affected by freshwater discharges under the tidal environment? Is the Lagrangian flow significantly different from the Eulerian residual flow?

Several Lagrangian experiments were conducted for the cases with tidal forcings and tidal forcings plus freshwater discharges. In each case, particles were initially released at the surface, middle depth, and bottom at SHW and SLW during spring tide in three selected regions: the main channel, the southern intertidal salt marsh, and the northern intertidal salt marsh. They were then tracked for 10 tidal cycles, with output of their locations every hour.

TIDAL FORCINGS ONLY

The experiments show that particle trajectories depend significantly on the release time and location. The particles, which are released initially at the surface at SHW in the southern salt marsh area, move quickly out of that area and enter the inner shelf during the ebb tidal period. When the tidal currents reverse, the particles move back into the main estuarine channel, with only a few moving back into the southern salt marsh area (Fig. 11a–e). When these particles are released at the surface at SLW, however, they tend to be washed out of the salt marsh and enter the inner shelf during the ebb tide (Fig. 11f–j). Similar differences are also observed in the northern salt marsh area. The particles, which are released initially at SHW, move periodically with tidal cycles over the salt marsh and inner shelf. They are quickly advected into the inner shelf during the ebb tidal period but

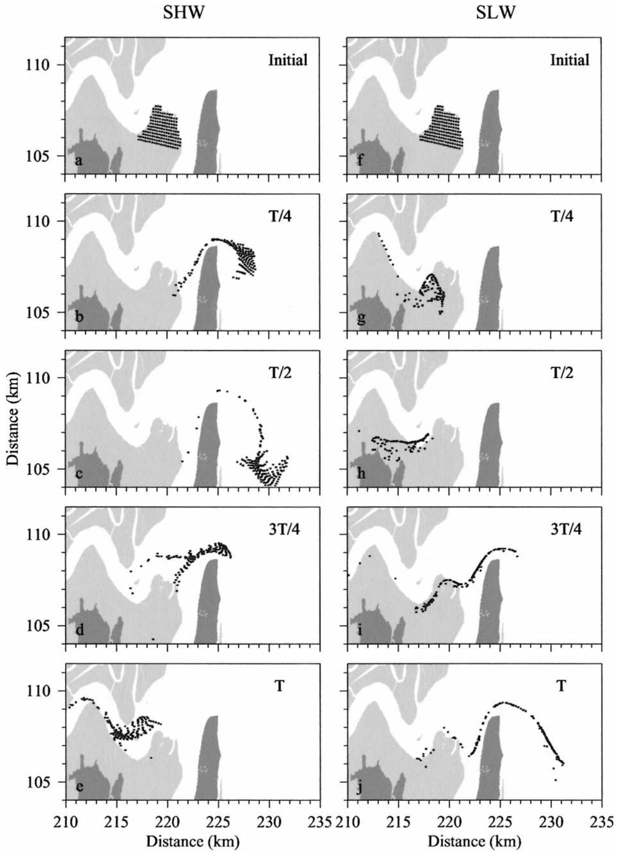

Fig. 11. The time sequences of the locations of particles released initially near the surface on the southern salt marsh area at SHW (left panel: a–e) and SLW (right panel: f–j) for the case with the tidal forcing only. Locations of particles are plotted every ¼ tidal period starting with the initial release. T represents the tidal period.

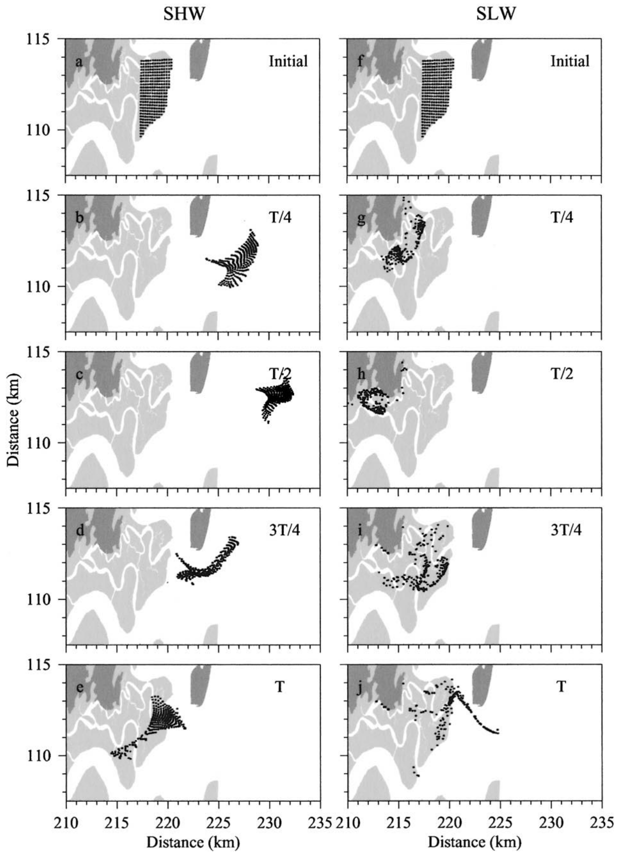

Fig. 12. The time sequences of the locations of particles released initially near the surface on the northern salt marsh area at SHW (left panel: a–e) and SLW (right panel: f–j) for the case with the tidal forcing only. Locations of particles are plotted every ¼ tidal period starting with the initial release. T represents the tidal period.

all returns to the salt marsh area during the flood tidal period (Fig. 12a–e). When these particles are initially released at SLW, they are trapped in the northern salt marsh area during the first few tidal cycles (Fig. 12f–j), except for a small portion that is advected into the inner shelf. These particles then move back and forth between the salt marsh and inner shelf.

These experiments demonstrate that water exchange over the intertidal salt marsh-estuary-inner shelf complex significantly differs between southern and northern salt marsh areas. In the southern salt marsh area, there is a net residual water flux into the inner shelf that tends to wash fluid particles out of the southern salt marsh area. In the northern salt marsh area, water exchange between the salt marsh and inner shelf is controlled by a periodic tidal advection, with a small net flux from one to the other. According to the law of mass conservation, a net loss of water from the southern salt marsh area to the inner shelf must be compensated for from other sources around that area. The trajectory of a selected individual particle shown in Fig. 13a suggests that the water in the upstream area of the estuary could be advected downstream to the southern salt marsh area to compensate for the water loss there.

The model does show an active cross-estuarine water exchange between southern and northern salt marsh areas. Good examples can be seen in Fig. 13a–c. The particle, which is initially released in the northern salt marsh area, is advected across the main channel of the river and enters in the southern salt marsh area (Fig. 13a). Particles that are released in the southern salt marsh area move across the river and enter the northern salt marsh area in a few tidal cycles (Fig. 13b,c). These particle trajectories imply that the water exchange process in the Satilla River estuary is completely a 3-D feature with a scale that covers the entire salt marsh-estuary complex. The transport of water, nutrients, and other biological variables estimated us-

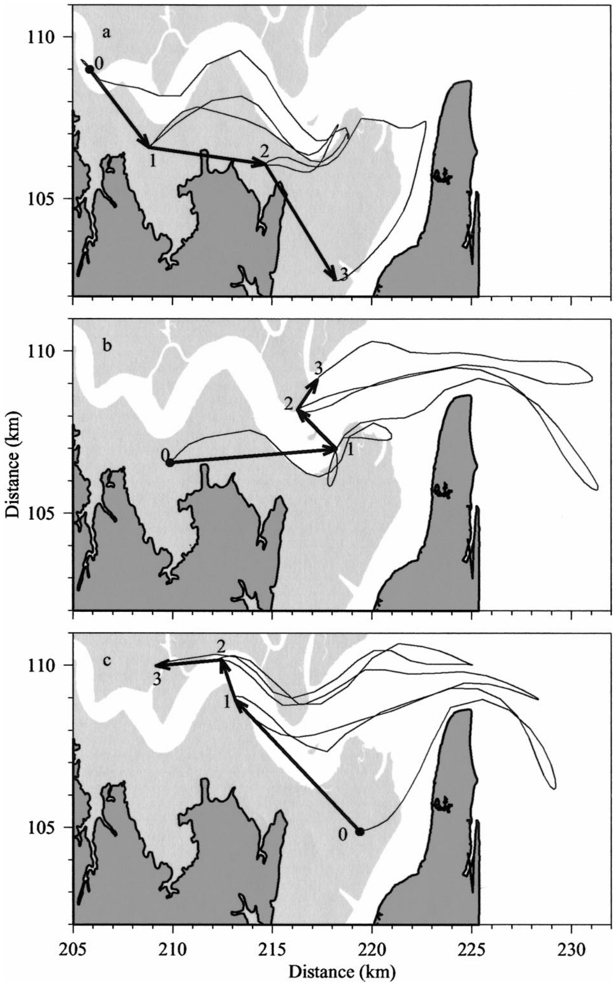

Fig. 13. Trajectories of selected particles released initially near the surface on the northern salt marsh (a) and southern salt marsh (b and c) for the case with the tidal forcing only. The number indicates the location after each tidal cycle from the initial release.

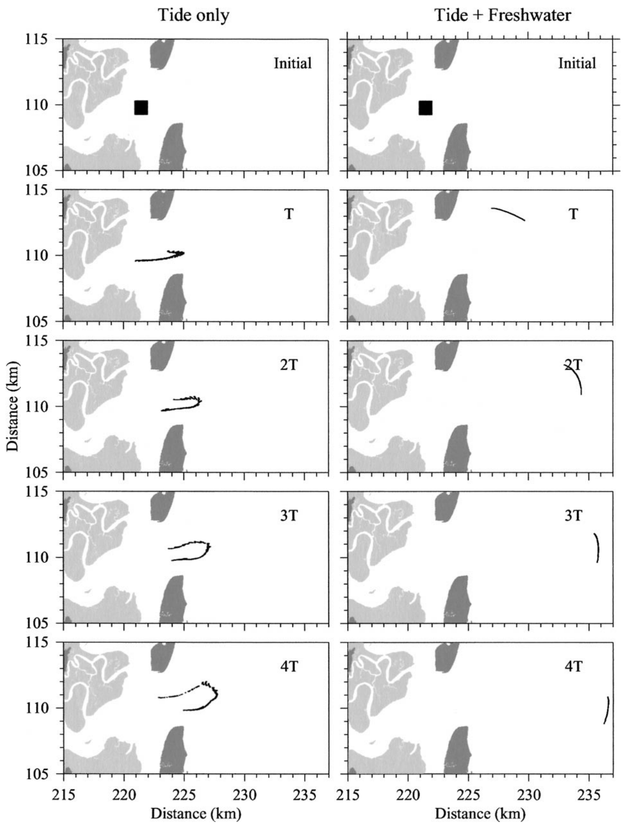

Fig. 14. The time sequences of the locations of particles released initially near the surface at SHW for the cases with tidal forcing only (left panel) and tide plus river discharge (right panel). The locations of particles are plotted every tidal cycles starting with the initial release.

ing a simple box model with a concept of the Eulerian flux would be very misleading.

EFFECTS OF THE FRESHWATER DISCHARGE

Particle trajectories are modified dramatically after freshwater discharge is added. An example could be seen by the comparison of particle trajectories between the cases with and without freshwater discharge (Fig. 14). Given the same initial positions of particles, the model-predicted particle trajectories differ significantly for these two cases. For the case with tidal forcing only, the particles remain near the mouth of the river after 4 tidal cycles, with a dominant stretch along the east-west axis and a laid-down U-shaped distribution. When freshwater discharge is added, these particles are advected away from their initial locations and form a line distribution after one tidal cycle. The distribution of the particles turns clockwise with time over those successive tidal cycles and the particles quickly move southward.

The difference in the particle trajectories between the cases with and without freshwater discharge was examined through a comparison of Lagrangian flow fields. To ensure that the residual Lagrangian current is well defined, the comparison was made for the cases with the M_2 tide only and the M_2 tide plus freshwater discharge. The residual Lagrangian current $\vec{V}_L$ is defined here as

$$\vec{V}_L = \frac{\vec{X}_T - \vec{X}_0}{T} \qquad (15)$$

where T is the M_2 tidal period, $\vec{X}_T$ and $\vec{X}_0$ are the end and start positions of a particle over T. Stokes' velocity is estimated by a difference between the Lagrangian and Eulerian residual currents defined as

$$\vec{V}_S = \vec{V}_L - \vec{V}_E \qquad (16)$$

where $\vec{V}_E$ is the Eulerian residual current (Chen et

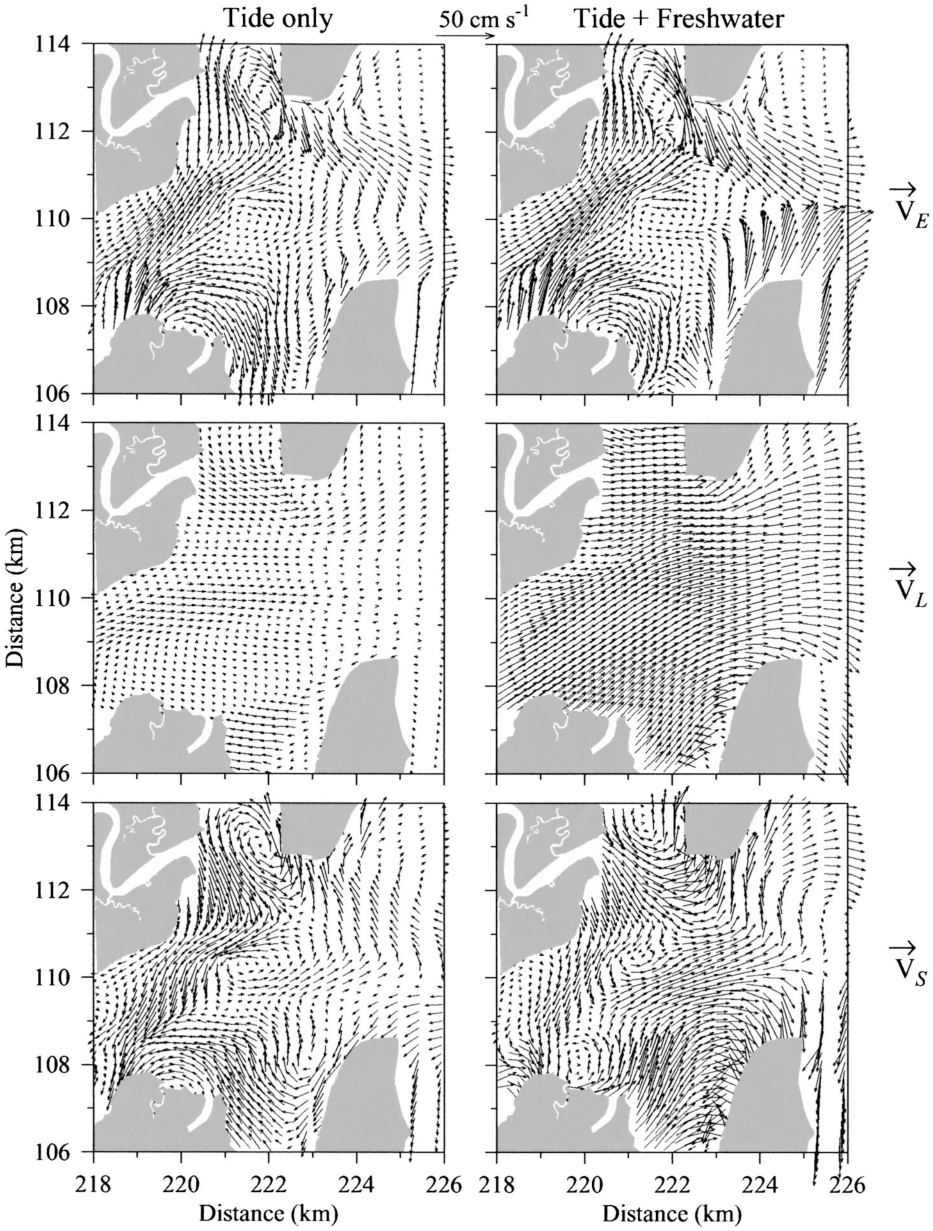

Fig. 15. Synoptic distributions of near-surface, tidal-cycle residual Eulerian ($\vec{V}_E$), Lagrangian ($\vec{V}_L$), and Stokes' ($\vec{V}_S$) current vectors for the cases with tidal forcing only (left panel) and tide plus river discharge (right panel).

al. in press). Particles are released at each grid point in both the horizontal and vertical where either $\bar{u}_E$ or $\bar{v}_E$ is computed. The synoptic distribution of the residual Lagrangian flow shown in Fig. 15 is based on the residual Lagrangian currents of surface particles after one tidal cycle.

The model-predicted residual Lagrangian and Eulerian flow fields significantly differ between the cases with and without freshwater discharge, even though the patterns of the Eulerian flow field are similar for both these cases. In the case with tidal forcing only, the model shows a weak residual Lagrangian flow in most areas of the Satilla River estuary. These residual currents of particles are characterized by multiple circulation cells, which favor chaotic water exchanges under a periodic tidal forcing (Chen and Beardsley 2002). In the case with tide plus freshwater discharge, a net offshore residual Lagrangian current is found in the main channel. This current decreases offshore, causing a weaker convergence zone in the center area of the outer part of the river mouth. Since the field of the Lagrangian flow is dominated by an offshore current that has multiple circulation cells, the particle motion should be more organized and predictable than particle motion in the case with tidal forcing only.

In the case with tidal forcing only, the weak residual Lagrangian current is due to the strong nonlinearity of the tidal current in the Satilla River estuary. In this case, the Stokes' current is the same order of magnitude as the Eulerian current. Since these two currents flow in opposite directions, their cancellation leads to a weak residual Lagrangian flow field. In the case with tidal forcing plus freshwater discharge, the residual Lagrangian current consists of two parts: tide-induced and buoyancy-induced flows. The relatively uniform distribution of the residual Lagrangian flow found in this case is a result of the nonlinear interaction between tidal and buoyancy flows.

Discussion

The flooding-draining process over the intertidal zone of the Satilla River estuary in Georgia is examined using the ECOM-si. A 3-D wet-dry point treatment method was developed and incorporated into the ECOM-si. The modified model was used to examine the physics of tidal waves, tidal and buoyancy-induced subtidal flows, and water exchanges over the intertidal salt marsh-estuary-inner shelf complex.

The model has provided a reasonable simulation of tidal elevations, tidal currents, and salinity in the Satilla River estuary. The model experiments show that the flooding-drying process plays a key role in the simulation of tidal current and transport in the Satilla River estuary. Ignoring this process leads to a 50% underestimation of tidal current amplitude compared with observations. The model-predicted tidal residual flow field is characterized by multiple eddy-like convergences and divergences. These complex residual circulation cells are intensified significantly when freshwater discharge is added. The physical mechanisms responsible for the formation of the eddy-like residual circulations are related to the nonlinear interaction of tidal currents over variable topography with superimposition of inertial curvature coastal effects, asymmetry of tidal currents over flood and ebb tidal phases, and an along-river baroclinic pressure gradient.

The trajectories of fluid particles depend on their initial release times and locations. Water exchanges over the salt marsh-estuary system differ significantly across the estuary, varying periodically on the northern side but tending to be washed out of the marsh zone on the southern side. An active cross-estuary water exchange could take place between the southern and northern salt marsh areas of the Satilla River. The Lagrangian residual currents generally flow in opposite direction from the Eulerian residual currents as a result of strong nonlinearity.

Our experiments have suggested that the dynamics and kinematics of the Satilla River estuary are controlled by the complex physical processes associated with tidal advection-mixing, buoyancy input (freshwater discharge), and topographic and tidal interaction. Because these processes have strong nonlinear coupling, they must be examined using a combined approach of modeling and observation. Since an active cross-estuary water exchange would occur over a short time scale of a few tidal cycles, attention must be paid to the Lagrangian water movement when biological and chemical samples are collected and analyzed. A 3-D estuarine model with inclusion of the flooding-drying process will be a useful tool for quantitatively examining the effect of nutrients and other organic matter loading into the Satilla River estuarine ecosystem.

It should be pointed out that the ECOM-si fails to resolve tidal creeks in the wet grid points because of the limitation of the orthogonal curvilinear coordinate transformation. A new unstructured grid, finite-volume coastal and estuarine circulation model (finite-volume coastal ocean model, FVCOM), which has been developed by Chen et al. (2003), has shown much promise in fitting of the complex geometry. It also shows reasonable efficiency regarding computation. A comparison between FVCOM and ECOM-si was recently made on the tidal simulation of the Satilla River estuary, which does show some modification of residual flow after including tidal creeks (Chen et al. 2003). Since the basic patterns of residual currents predicted by these two models remain unchanged, our current studies using ECOM-si as a first step to examine the complex current system in the Satilla River estuary is still robust.

ACKNOWLEDGMENTS

This research was supported by the Georgia Sea Grant College Program under grant numbers NA26RG0373 and NA66RG0282. We thank Dr. Jack Blanton of the Skidaway Institute of Oceanography (SKIO) for providing the observational data used for validating the model. These observations were collected through support to SKIO provided by the Georgia Coastal Zone Management Program (Grant No. RR100-279/9262764), the National Science Foundation (LMER Grant No. DEB-9412089 and LTER Grant No. OCE-9982133), and a grant from the Georgia General Assembly. We thank Dr. Mac Rawson for his encouragement and help in project organization. The 2-m elevation line was obtained from the GIS database created by Dr. Alice Chalmers; her help is greatly appreciated and the model configuration would have been impossible without her kind assistance. Finally, we want to thank George Davidson, who kindly provided editorial assistance on this manuscript.

Literature Cited

Alber, M. and J. E. Sheldon. 1999. Use of a data-specific method to examine variability in the flushing times of Georgia estuaries. *Estuarine, Coastal and Shelf Science* 49:469–482.

Austria, P. M. and A. A. Aldama. 1990. Adaptive mesh scheme for free surface flows with moving boundaries, p. 456–460. *In* G. Gambolati, A. Rinaldo, C. A. Brebbiam, W. G. Fray, and G. F. Pinder (eds.), Computational Methods in Surface Hydrology. Springer-Verlag, New York.

Blanton, J. O. 1996. Reinforcement of gravitational circulation by wind. Buoyancy effects on coastal and estuarine dynamics, coastal estuarine studies. American Geophysical Union, Washington, D.C. 53:47–58.

Blanton, J. O., C. Alexander, M. Alber, and G. Kineke. 1999. The mobilization and deposition of mud deposits in a coastal plain estuary. *Limnologica* 29:293–300.

Blumberg, A. F. 1993. A primer of ECOM3D-si. Technical report. HydroQual, Inc., Mahwah, New Jersey.

Blumberg, A. F. and G. L. Mellor. 1987. A description of a three-dimensional coastal ocean circulation model, p. 1–16. *In* N. Heaps (ed.), Three-Dimensional Coastal Ocean Models. American Geophysical Union, Washington, D.C.

Casulli, V. 1990. Semi-implicit finite-difference methods for the two-dimensional shallow water equations. *Journal of Computational Physics* 86:56–74.

Casulli, V. and E. Cattani. 1994. Stability, accuracy and efficiency of a semi-implicit method for three-dimensional shallow water flow. *Computers and Mathematics with Application* 27:99–112.

Casulli, V. and R. T. Cheng. 1991. A semi-implicit finite-difference model for three-dimensional tidal circulation, p. 620–631. *In* M. Spaulding, C. Swanson, R. Cheng, A. Blumberg, and K. Bedford (eds.), Proceeding of 2nd International Conference on Estuarine and Coastal Modeling. American Society of Civil Engineers, Tampa, Florida.

Casulli, V. and R. T. Cheng. 1992. Semi-implicit finite-difference methods for three-dimensional shallow-water flow. *International Journal for Numerical Methods in Fluids* 15:629–648.

Chadwick, D. B. and J. L. Largier. 1999. The influence of tidal range on the exchange between San Diego Bay and the ocean. *Journal of Geophysical Research* 104:29885–29899.

Chen, C. and R. C. Beardsley. 1995. A numerical study of stratified tidal rectification over finite-amplitude banks. I. Symmetric banks. *Journal of Physical Oceanography* 25:2090–2110.

Chen, C. and R. C. Beardsley. 1998. Tidal mixing and cross-frontal particle exchange over a finite amplitude asymmetric bank: A model study with application to Georges Bank. *Journal of Marine Research* 56:1163–1201.

Chen, C. and R. C. Beardsley. 2002. Cross-frontal water exchange on Georges Bank: Some results from an U.S. GLOBEC/Georges Bank program model study. *Journal of Oceanography* 58:403–420.

Chen, C., R. C. Beardsley, and R. Limeburner. 1995. A numerical study of stratified tidal rectification over finite-amplitude banks. II. Georges Bank. *Journal of Physical Oceanography* 25:2111–2128.

Chen, C., H. Liu, and R. C. Bearsley. 2003. An unstructured grid, finite-volume, three-dimensional, primitive equations ocean model: Application to coastal ocean and estuaries. *Journal of Atmospheric and Oceanic Technology* 20:159–186.

Chen, C., Q. Xu, R. C. Beardsley, and P. S. Franks. In press. Model study of the cross-frontal water exchange on Georges Bank: A 3-D lagrangian experiment. *Journal of Geophysical Research.*

Chen, C., L. Zheng, and J. O. Blanton. 1999. Physical processes controlling the formation, evolution, and perturbation of the low-salinity front in the inner shelf off the southeastern United States: A modeling study. *Journal of Geophysical Research* 104:1259–1288.

Cheng, R. T., V. Casulli, and J. W. Gartner. 1993. Tidal, residual, intertidal mudflat (TRIM) model and its applications to San Francisco Bay, California. *Estuarine, Coastal and Shelf Science* 36:235–280.

Davies, A. M., J. E. Jones, and J. Xing. 1997. Review of recent developments in tidal hydrodynamic modeling. I: Spectral models. *Journal of Hydraulic Engineering* 123:278–292.

Emery, K. O. 1967. Estuaries and lagoons in relationship to continental shelves, p. 9–11. *In* G. H. Lauff (ed.), Estuaries, American Association of Advanced Scientific Publication 83. Washington, D.C.

Fischer, H. B., B. E. List, R. C. Y. Kuo, J. Imberger, and N. H. Brooks. 1979. Mixing in Inland and Coastal Waters. Academic Press, New York.

Flather, R. A. and N. S. Heaps. 1975. Tidal computations for Morecambe Bay. *Geophysical Journal of the Royal Astronomical Society* 42:489–517.

Foreman, M. G. G. 1978. Manual for tidal analysis and prediction. Pacific Marine Science Report 78-6. Institute of Ocean Sciences, Particia Bay, Sidney, British Columbia.

Galperin, B., L. H. Kantha, S. Hassid, and A. Rosati. 1988. A quasi-equilibrium turbulent energy model for geophysical flows. *Journal of Atmospheric Science* 45:55–62.

Geyer, W. R. 1993. Three-dimensional tidal flow around headlands. *Journal of Geophysical Research* 98:955–966.

Haidvogel, D. B., J. L. Wilkin, and R. Young. 1991. A semi-spectral primitive equation ocean circulation model using vertical sigma and orthogonal curvilinear horizontal coordinates. *Journal of Computational Physics* 94:151–185.

Hervouet, J. M. and J. M. Janin. 1994. Finite-element algorithms for modeling flood propagation, p. 102–113. *In* P. Molinaro and L. Natale (eds.), Modeling of Flood Propagation Over Initially Dry Areas. American Society of Civil Engineers, New York.

Huthnance, J. M. 1973. Tidal current asymmetries over Norfolk Sandbank. *Estuarine and Coastal Marine Science* 1:89–99.

Imasato, N. 1983. What is tide-induced residual current? *Journal of Physical Oceanography* 13:1307–1317.

Ip, J. T. C., D. R. Lynch, and C. T. Friedrichs. 1998. Simulation of estuarine flooding and dewatering with application to Great Bay, New Hampshire. *Estuarine, Coastal and Shelf Science* 47:119–141.

Johns, B., S. K. Dube, P. C. Sinha, U. C. Mohanty, and A. D. Rao. 1982. The simulation of a continuously deforming lateral boundary in problems involving the shallow water equations. *Computer and Fluids* 10:105–116.

Kapolnai, A., F. E. Werner, and J. B. Blanton. 1996. Circulation, mixing, and exchange processes in the vicinity of tidal inlets: A numerical study. *Journal of Geophysical Research* 101:14253–14268.

Leendertse, J. J. 1970. A water-quality simulation model for well-mixed estuaries and coastal seas: Principles of computation, Report RM-6230-RC, Volume I. Rand Corporation, Santa Monica, California.

Leendertse, J. J. 1987. Aspects of SIMSYS2D, a system for two-dimensional flow computation. Report R-3572-USGS. Rand Corporation, Santa Monica, California.

Loder, J. W. 1980. Topographic rectification of tidal currents on the sides of Georges Bank. *Journal of Physical Oceanography* 10:1399–1416.

Lynch, D. R. and W. G. Gray. 1980. Finite element simulation of flow in deforming regions. *Journal of Computational Physics* 36:135–153.

Lynch, D. R. and F. E. Werner. 1987. Three-dimensional hydrodynamics on finite elements. Part I: Linearized harmonic model. *International Journal for Numerical Methods in Fluids* 7:871–909.

Mellor, G. L. and T. Yamada. 1982. Development of a turbulence closure model for geophysical fluid problems. *Review of Geophysics* 20:851–875.

MOORE, W. S. 1996. Large groundwater inputs to coastal waters revealed by $_{226}$Ra enrichment. *Nature* 380:612–614.

RIDD, P. V., T. STIEGLITZ, AND P. LARCOMBE. 1998. Density-driven secondary circulation in a tropical mangrove estuary. *Estuarine, Coastal and Shelf Science* 47:621–632.

SHI, F. 1995. On moving boundary numerical models of coastal sea dynamics. Ph.D. Dissertation, Ocean University of Qingdao, Qingdao, China.

SIDÉN, G. L. D. AND D. R. LYNCH. 1988. Wave equation hydrodynamics on deforming elements. *International Journal for Numerical Methods in Fluids* 8:1071–1093.

SMOLARKIEWICZ, P. K. 1984. A fully multidimensional positive definite advection transport algorithm with small implicit diffusion. *Journal of Computational Physics* 54:325–362.

WHELESS, G. H. AND A. VALLE-LEVINSON. 1996. A modeling study of tidally driven estuarine exchange through a narrow inlet onto a sloping shelf. *Journal of Geophysical Research* 101:25675–25687.

ZHENG, L. 1999. A three-dimensional modeling study of estuarine system: An application to Satilla River, Georgia. M.S. Thesis, University of Georgia, Athens, Georgia.

ZIMMERMAN, J. T. F. 1978. Topographic generation of residual circulation by oscillatory tidal currents. *Geophysical and Astrophysical Fluid Dynamics* 11:35–47.

Received for consideration, December 1, 2000
Revised, June 5, 2002
Accepted for publication, July 9, 2002